

Fast algorithm for the analysis of scattering by dielectric rough surfaces

Vikram Jandhyala,* Balasubramaniam Shanker, Eric Michielssen,[†] and Weng C. Chew

*Center for Computational Electromagnetics, Department of Electrical and Computer Engineering,
1406 West Green Street, University of Illinois at Urbana-Champaign, Urbana, Illinois 61801*

Received July 11, 1997; revised manuscript received January 5, 1998; accepted February 19, 1998

A novel multilevel algorithm to analyze scattering from dielectric random rough surfaces is presented. This technique, termed the steepest-descent fast-multipole method, exploits the quasi-planar nature of dielectric rough surfaces to expedite the iterative solution of the pertinent integral equation. A combination of the fast-multipole method and Sommerfeld steepest-descent-path integral representations is used to efficiently compute electric and magnetic fields that are due to source distributions residing on the rough surface. The CPU time and memory requirements of the technique scale linearly with problem size, thereby permitting the rapid analysis of scattering by large dielectric surfaces and permitting Monte Carlo simulations with realistic computing resources. Numerical results are presented to demonstrate the efficacy of the steepest-descent fast-multipole method. © 1998 Optical Society of America [S0740-3232(98)00407-4]

OCIS codes: 290.5880, 000.4430.

1. INTRODUCTION

The analysis of electromagnetic scattering by perfectly conducting and dielectric random rough surfaces is a research topic of fervent current interest.¹ Applications² arise in diverse areas, including remote sensing, long-range communications, and surface physics. Specific examples include the modeling of soil, ocean, and ice surfaces; the simulation of quasi-random gratings for infrared detectors; and the analysis and design of antireflection coatings for optical systems.

The analysis of three-dimensional scattering from two-dimensional rough surfaces is a large-scale vector problem whose solution requires efficient and accurate numerical techniques. The most popular approaches for analyzing rough-surface scattering rely on integral equation formulations and method-of-moments- (MoM-) based solution techniques. For large rough surfaces, solution of the MoM equations by direct matrix inversion is impractical owing to the large CPU time and memory requirements associated with this procedure. The iterative solution of the MoM system is also a time-consuming process, with both the number of operations per iteration and the memory cost associated with storing the matrix scaling as $O(N^2)$, where N is the dimension of the system. To expedite the iterative solution of electromagnetic scattering problems, researchers have exploited the underlying structure of the Green's function kernel and have developed techniques that facilitate the fast computation of MoM matrix-vector products.³⁻¹³ Two efficient multilevel techniques are specifically geared toward the analysis of scattering from rough surfaces. These methods have been used to compute the matrix-vector product in $O(N \log N)$ operations by taking advantage of the fact that rough surfaces are nearly planar (or quasi planar), to alleviate the CPU time and memory burden. The first of these techniques is the sparse-matrix flat-surface iterative approach,¹⁴ which relies on Taylor-series expansions

and the fast Fourier transform for accelerating the matrix-vector product. This method has been applied to the analysis of scattering from both perfectly conducting and dielectric rough surfaces.¹⁵ The second approach combines the fast-multipole method (FMM) with the fast Fourier transform,¹⁶ and has been used for analyzing scattering from perfectly conducting rough surfaces. Other prevalent MoM-based complexity reducing techniques for rough-surface scattering analysis include the method of multiple ordered interactions¹⁷ and a direct technique that utilizes reduced source representations.¹⁸

We recently reported the development of the steepest-descent fast-multipole method (SDFMM)¹⁹ for the analysis of scattering from perfectly conducting rough surfaces. The SDFMM, a numerically rigorous technique, exploits the quasi planarity of rough surfaces to reduce the computational costs per iteration and memory requirements to $O(N)$. In this paper the SDFMM is extended to the more general and complex problem of scattering by dielectric rough surfaces. A PMCHW formulation²⁰ (after Poggio, Miller, Chang, Harrington, and Wu) is utilized, and terms arising in an MoM matrix-vector product are cast in the form of discrete inhomogeneous plane-wave expansions arising from the representation of the pertinent Green's function along steepest-descent paths and from the use of the FMM. Both electric and magnetic surface currents, as opposed to the electric-current-based formulation for analyzing perfectly conducting surfaces reported earlier,¹⁹ need to be incorporated into the multilevel formulation, and independent fast-multipole and steepest-descent representations are required for each dielectric region. The SDFMM permits the solution of extremely large dielectric rough surfaces and makes Monte Carlo simulations feasible within realistic times. Surfaces modeled with as many as 191,530 current basis functions have been solved with this approach.

This paper is organized as follows: Section 2 describes

dielectric rough-surface modeling and the PMCHW formulation of the scattering problem. In Section 3 the theoretical formulation of the SDFMM is developed and applied to the PMCHW equations. The computational complexity of the technique and the memory requirements are also discussed. Section 4 describes numerical results, and our conclusions are presented in Section 5.

2. INTEGRAL EQUATION FORMULATION FOR SCATTERING BY DIELECTRIC ROUGH SURFACES

One often analyzes the scattering properties of a class of rough surfaces by performing a Monte Carlo simulation on a statistical ensemble of finite rough surfaces. These surfaces are generated with the surface height z assumed to be a random function of the lateral coordinates x and y , with a specified distribution. For example, Gaussian rough surfaces,^{16,21} which are considered in this paper, are characterized by height profiles $z(x, y)$ that satisfy

$$\langle z(x, y) \rangle = 0, \quad (1a)$$

$$\langle z(x, y)z(x', y') \rangle = \sigma^2 \exp\{-[(x - x')^2 + (y - y')^2]/l_c^2\}, \quad (1b)$$

where $\langle \cdot \rangle$ denotes an ensemble average, σ is the rough surface variance, and l_c is the correlation length.

To formulate integral equations for a dielectric rough surface, we follow the approach of Refs. 20 and 22. Throughout this paper, a temporal dependency of $\exp\{-i\omega t\}$ is assumed and suppressed. A finite rough surface S , of dimensions $L \times L$, formed at the interface of two dielectric half-spaces is shown in Fig. 1. Incident electric and magnetic fields $\mathbf{E}^{\text{inc}}(\mathbf{r})$ and $\mathbf{H}^{\text{inc}}(\mathbf{r})$ excite S from Region 1, and equivalent electric and magnetic surface currents $\mathbf{J}(\mathbf{r})$ and $\mathbf{M}(\mathbf{r})$ are impressed on the rough surface. In what follows, ϵ_q and μ_q , with $q = 1, 2$, rep-

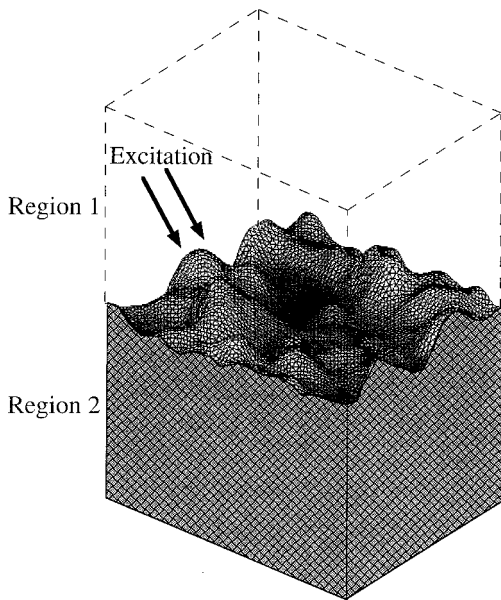


Fig. 1. Rough surface formed at the interface of two regions. Regions 1 and 2 have distinct permittivities. Typically, Region 1 is free space.

resent the permittivity and the permeability, respectively, of the half-spaces separated by the surface S . Also, $k_q = \omega(\epsilon_q\mu_q)^{1/2}$, and $\eta_q = (\mu_q/\epsilon_q)^{1/2}$. For a finite surface sample to be an accurate representation of an essentially infinite interface, a spatially limited excitation is employed so that edge effects are avoided. Specifically, a Gaussian-weighted superposition of plane waves^{16,21} is used:

$$\begin{aligned} \mathbf{E}^{\text{inc}}(\mathbf{r}) &= \frac{2\pi W^2}{L^2} \sum_{|\mathbf{K}| \leq k_1} \hat{\mathbf{e}}^{\text{inc}}(\mathbf{K}, k_z) \\ &\quad \times \exp(i\mathbf{K} \cdot \boldsymbol{\rho}) \exp(-ik_z z) \\ &\quad \times \exp(-|\mathbf{K} - \mathbf{K}_0|^2 W^2/2), \end{aligned} \quad (2)$$

$$\hat{\mathbf{e}}^{\text{inc}}(K_x, K_y, k_z) = \frac{1}{(K_x^2 + k_z^2)^{1/2}} (k_z, 0, K_x), \quad (3)$$

where \mathbf{K}_0 is the average wave vector in the transverse plane. Also, $\mathbf{r} = \hat{\mathbf{z}}z + \boldsymbol{\rho}$ and $\mathbf{K} = (K_x, K_y)$, with K_x and K_y being multiples of $2\pi/L$. The dispersion relation $K_x^2 + K_y^2 + k_z^2 = k_1^2$ is satisfied. Typically, $W = L/4$.¹⁶ To obtain \mathbf{J} and \mathbf{M} , the PMCHW formulation enforces the continuity of the tangential electric- and magnetic-field components across S :

$$\mathbf{E}^{\text{inc}}(\mathbf{r})|_{\text{tan}} = (L_1 + L_2)\mathbf{J}(\mathbf{r})|_{\text{tan}} - (K_1 + K_2)\mathbf{M}(\mathbf{r})|_{\text{tan}} \quad (4a)$$

$$\begin{aligned} \mathbf{H}^{\text{inc}}(\mathbf{r})|_{\text{tan}} &= (K_1 + K_2)\mathbf{J}(\mathbf{r})|_{\text{tan}} \\ &\quad + \left(\frac{1}{\eta_1^2} L_1 + \frac{1}{\eta_2^2} L_2 \right) \mathbf{M}(\mathbf{r})|_{\text{tan}} \end{aligned} \quad (4b)$$

where the operators L_q and K_q are defined by

$$\begin{aligned} L_q \mathbf{X}(\mathbf{r}) &= \int_S ds' \left[-i\omega\mu_q \mathbf{X}(\mathbf{r}') \right. \\ &\quad \left. + \frac{-i}{\omega\epsilon_q} \nabla \nabla' \cdot \mathbf{X}(\mathbf{r}') \right] g_q(\mathbf{r}, \mathbf{r}'), \end{aligned} \quad (4c)$$

$$K_q \mathbf{X}(\mathbf{r}) = \int_S ds' \mathbf{X}(\mathbf{r}') \times \nabla g_q(\mathbf{r}, \mathbf{r}'), \quad (4d)$$

and $g_q(\mathbf{r}, \mathbf{r}')$ is the scalar Green's function

$$g_q(\mathbf{r}, \mathbf{r}') = \frac{\exp(ik_q|\mathbf{r} - \mathbf{r}'|)}{4\pi|\mathbf{r} - \mathbf{r}'|}. \quad (4e)$$

The solution of the PMCHW [Eq. (4)] yields the electric and magnetic surface current densities $\mathbf{J}(\mathbf{r})$ and $\mathbf{M}(\mathbf{r})$. These current densities can be used to evaluate the scattered field $\mathbf{E}^{\text{scat}}(\mathbf{r})$ required in the computation of the bistatic radar cross section (RCS), which is given by

$$\sigma_{\gamma\delta}(\theta, \phi) = \lim_{r \rightarrow \infty} \frac{4\pi r^2 S_\delta(\theta, \phi, \mathbf{r})}{P_\gamma^{\text{inc}}}. \quad (5)$$

Here P_γ^{inc} is the incident beam power, $S_\delta(\mathbf{r})$ is the scattered power density, and γ and δ denote the polarization of the incident and the considered scattered electric field, respectively. In a Monte Carlo simulation the variance of $\mathbf{E}^{\text{scat}}(\mathbf{r})$ over an ensemble of rough surfaces possessing

the same l_c and σ is used to compute the noncoherent part of the bistatic scattering coefficient.^{2,16,23}

3. STEEPEST-DESCENT FAST-MULTIPOLE METHOD

To solve the PMCHW [Eq. (4)], the unknown current densities $\mathbf{J}(\mathbf{r})$ and $\mathbf{M}(\mathbf{r})$ are approximated in terms of linear combinations of a set of basis functions \mathbf{j}_n , $n = 1, \dots, N$, as

$$\mathbf{J}(\mathbf{r}) \cong \sum_{n=1}^N I_n^1 \mathbf{j}_n(\mathbf{r}), \quad (6a)$$

$$\mathbf{M}(\mathbf{r}) \cong \sum_{n=1}^N I_n^2 \mathbf{j}_n(\mathbf{r}). \quad (6b)$$

Substituting relations (6a) and (6b) into Eqs. (4a) and (4b) and testing the latter two equations with functions \mathbf{f}_m , for $m = 1, \dots, N$, results in a $2N \times 2N$ system of equations:

$$\bar{\mathbf{Z}} \cdot \mathbf{I} = \mathbf{V}. \quad (7)$$

Here the MoM matrix $\bar{\mathbf{Z}}$ has the form

$$\bar{\mathbf{Z}} = \begin{bmatrix} \bar{\mathbf{Z}}^{11} & \bar{\mathbf{Z}}^{12} \\ \bar{\mathbf{Z}}^{21} & \bar{\mathbf{Z}}^{22} \end{bmatrix}, \quad (8a)$$

with the entries of the four $N \times N$ submatrices given by

$$Z_{mn}^{11} = \langle \mathbf{f}_m, (L_1 + L_2) \mathbf{j}_n \rangle, \quad (8b)$$

$$Z_{mn}^{12} = \langle \mathbf{f}_m, -(K_1 + K_2) \mathbf{j}_n \rangle, \quad (8c)$$

$$Z_{mn}^{21} = \langle \mathbf{f}_m, (K_1 + K_2) \mathbf{j}_n \rangle, \quad (8d)$$

$$Z_{mn}^{22} = \left\langle \mathbf{f}_m, \left(\frac{1}{\eta_1^2} L_1 + \frac{1}{\eta_2^2} L_2 \right) \mathbf{j}_n \right\rangle. \quad (8e)$$

Also, the vector of coefficients \mathbf{I} is

$$\mathbf{I} = \begin{pmatrix} \mathbf{I}^1 \\ \mathbf{I}^2 \end{pmatrix}, \quad (9)$$

and the excitation vector \mathbf{V} is given by

$$\mathbf{V} = \begin{pmatrix} \mathbf{V}^1 \\ \mathbf{V}^2 \end{pmatrix}, \quad (10a)$$

where

$$V_m^1 = \langle \mathbf{f}_m, \mathbf{E}^{\text{inc}}(\mathbf{r}) \rangle, \quad (10b)$$

$$V_m^2 = \langle \mathbf{f}_m, \mathbf{H}^{\text{inc}}(\mathbf{r}) \rangle. \quad (10c)$$

The Rao–Wilton–Glisson basis²⁴ is chosen for both \mathbf{j}_n and \mathbf{f}_m .

An iterative solution of Eq. (7) is expensive, since both the CPU time per iteration and the memory scale as $O(N^2)$. For large-scale problems one needs to develop efficient fast algorithms to alleviate the computational burden. To this end the SDFMM is introduced, based on our earlier work on electric-field integral equations for perfectly conducting surfaces.¹⁹ The key differences between the dielectric problem considered here and those considered in our previous work are that (i) both electric and magnetic currents feature in the equations, (ii) both

electric and magnetic fields need to be evaluated in a multilevel manner, and (iii) each dielectric half-space requires a different Green's function and therefore has to be treated separately.

The SDFMM is an algorithm that facilitates the computation of electromagnetic fields at N locations on a quasi-planar surface that are due to N sources on that surface with an operation count that scales more favorably than the $O(N^2)$ measure of a classical evaluation scheme. This multilevel technique relies on a recursive grouping of sources and observers similar to that used in a standard multilevel FMM.^{10,7} However, in contrast to the FMM, the SDFMM exploits the quasi-planar nature of the surface through a steepest-descent-path representation of the Green's function, thus eventually leading to an $O(N)$ algorithm, as opposed to the $O(N \log N)$ cost of an FMM employed for the same purpose.

In a single-level implementation of the dielectric SDFMM, the rough surface is embedded in a block of dimensions $L \times L \times H$, where $H = 2 \max[|z(x, y)|]$. This block is divided into smaller blocks of dimensions $l \times l \times H$, as shown in Fig. 2. No partitioning is carried out in the z direction, and z coordinates of the block centers are determined by the average heights of the rough-surface portion that is present in each block. A matrix element is classified as a near-field element if the corresponding basis and testing functions reside in blocks that are separated by less than a prespecified number of blocks. All other elements are termed far-field elements. This classification is used to formally decompose the impedance matrix $\bar{\mathbf{Z}}$ as

$$\bar{\mathbf{Z}} = \bar{\mathbf{Z}}' + \bar{\mathbf{Z}}'', \quad (11)$$

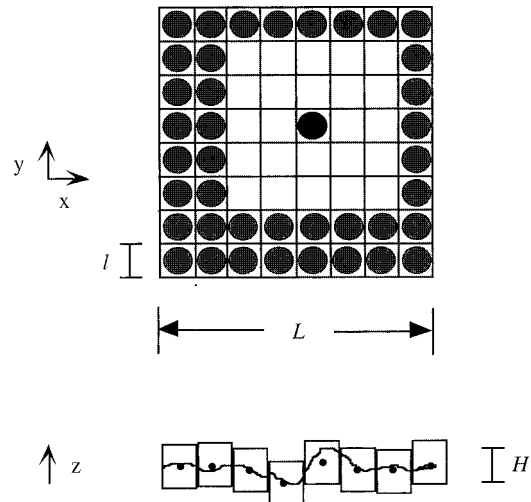


Fig. 2. SDFMM far-field interactions in a single-level implementation. The dielectric rough-surface of size $L \times L$ has been divided into blocks of surface dimensions $l \times l$. These blocks have the z coordinate of their center (small dark circles) determined by the mean height of the portion of the rough surface they enclose. These circles represent plane-wave expansions. The block with its expansion shown as a black circle is in the far field of the blocks with expansions represented by gray circles. The maximum peak-to-peak height of the rough surface is H .

where $\bar{\mathbf{Z}}'$ and $\bar{\mathbf{Z}}''$ contain near- and far-field interactions, respectively.

In the SDFMM the action of $\bar{\mathbf{Z}}'$ on a vector is computed classically. However, we compute the product of $\bar{\mathbf{Z}}''$ with a vector indirectly and rapidly, without ever generating the matrix. This is achieved as follows. The three-dimensional dynamic scalar Green's function $g_q(\mathbf{r}, \mathbf{r}')$ is first expressed in a contour integral form by means of the Sommerfeld identity²⁵:

$$\frac{\exp(ik_q|\mathbf{r} - \mathbf{r}'|)}{4\pi|\mathbf{r} - \mathbf{r}'|} = \frac{i}{8\pi} \int_{-\infty}^{\infty} dk_{zq} \exp[ik_{zq}(z - z')] H_0^{(1)} \times (k_{\rho q}|\boldsymbol{\rho} - \boldsymbol{\rho}'|), \quad (12)$$

where $k_{\rho q} = (k_q^2 - k_{zq}^2)^{1/2}$, $\mathbf{r} = \hat{\mathbf{z}}z + \boldsymbol{\rho}$, and $\mathbf{r}' = \hat{\mathbf{z}}z' + \boldsymbol{\rho}'$. The Hankel function can be factored as

$$H_0^{(1)}(k_{\rho q}|\boldsymbol{\rho} - \boldsymbol{\rho}'|) = \hat{H}_0^{(1)}(k_{\rho q}|\boldsymbol{\rho} - \boldsymbol{\rho}'|) \exp\{ik_{\rho q}|\boldsymbol{\rho} - \boldsymbol{\rho}'|\}, \quad (13)$$

Let $\mathbf{r}_c = \hat{\mathbf{z}}z_c + \boldsymbol{\rho}_c$ and $\mathbf{r}'_c = \hat{\mathbf{z}}z'_c + \boldsymbol{\rho}'_c$ be the coordinates of the centers of the source and the observation blocks, respectively, and let $\mathbf{r}_1 = \hat{\mathbf{z}}z_c + \boldsymbol{\rho}$ and $\mathbf{r}'_1 = \hat{\mathbf{z}}z'_c + \boldsymbol{\rho}'$. We can write Eq. (12) as

$$g_q(\mathbf{r}, \mathbf{r}') = -\frac{i}{8\pi} \int_{-\infty}^{\infty} dk_{zq} \exp[ik_{zq}(\delta z - \delta z')] \times \hat{H}_0^{(1)}(k_{\rho q}|\boldsymbol{\rho} - \boldsymbol{\rho}'|) \exp[ik_{\rho q}|\boldsymbol{\rho} - \boldsymbol{\rho}'| + ik_{zq}(z_c - z'_c)], \quad (14)$$

where $\delta z = z - z_c$ and $\delta z' = z - z'_c$. By letting $k_{zq} = k_q \cos \alpha$ and $k_{\rho q} = k_q \sin \alpha$, we have

$$g_q(\mathbf{r}, \mathbf{r}') = -\frac{ik_q}{8\pi} \int_{\Gamma} d\alpha \sin \alpha \exp[ik_{zq}(\delta z - \delta z')] \times \hat{H}_0^{(1)}(k_q \sin \alpha |\boldsymbol{\rho} - \boldsymbol{\rho}'|) \times \exp[ik_q|\mathbf{r}_1 - \mathbf{r}'_1| \cos(\alpha - \theta_1)], \quad (15)$$

where $\theta_1 = \cot^{-1}[(z_c - z'_c)/|\boldsymbol{\rho} - \boldsymbol{\rho}'|]$, with $0 \leq \theta_1 \leq \pi$. The saddle point is at $\alpha = \theta_1$. In anticipation of the aggregation of source points within a source block and the disaggregation of field-evaluation points within an observation block, we choose a particular steepest-descent path (SDP) defined by

$$ik_q|\mathbf{r}_1 - \mathbf{r}'_1| \cos(\alpha - \theta_c) = ik_q|\mathbf{r}_1 - \mathbf{r}'_1| - s^2, \quad (16)$$

where $\theta_c = \cot^{-1}[(z_c - z'_c)/|\boldsymbol{\rho}_c - \boldsymbol{\rho}'_c|]$. On deforming the integrand along the SDP, we obtain

$$g_q(\mathbf{r}, \mathbf{r}') = -\frac{ik_q}{8\pi} \exp(ik_q|\mathbf{r}_1 - \mathbf{r}'_1|) \times \int_{-\infty}^{\infty} ds \frac{d\alpha}{ds} \sin \alpha \exp\{ik_{zq}(\delta z - \delta z')\} \times \hat{H}_0^{(1)}(k_q \sin \alpha |\boldsymbol{\rho} - \boldsymbol{\rho}'|) \times \exp\{ik_q|\mathbf{r}_1 - \mathbf{r}'_1| [\cos(\alpha - \theta_1) - \cos(\alpha - \theta_c)]\} \exp\{-s^2\}. \quad (17)$$

The function $\hat{H}_0^{(1)}(k_q \sin \alpha |\boldsymbol{\rho} - \boldsymbol{\rho}'|) \exp\{ik_q|\mathbf{r}_1 - \mathbf{r}'_1| [\cos(\alpha - \theta_1) - \cos(\alpha - \theta_c)]\}$ varies slowly for large arguments. Efficient quadrature rules that require a small number $n_{(sd),q}$ of points can be developed for computing the above integral, as the integrand decays exponentially and both δz and $\delta z'$ are small for a quasi-planar structure. The above integral can then be approximated as

$$g_q(\mathbf{r}, \mathbf{r}') = \frac{i}{8\pi} \exp(ik_q|\mathbf{r}_1 - \mathbf{r}'_1|) \times \sum_{j=1}^{n_{(sd),q}} w_{jq}^{(sd)} k_{\rho q}^{(j)} \exp[ik_{zq}^{(j)}(\delta z - \delta z')] \times \hat{H}_0^{(1)}(k_{\rho q}^{(j)}|\boldsymbol{\rho} - \boldsymbol{\rho}'|) \exp\{ik_q|\mathbf{r}_1 - \mathbf{r}'_1| \times [\cos(\alpha_j - \theta_1) - \cos(\alpha_j - \theta_c)]\} \exp(-s_{jq}^2), \quad (18)$$

where $k_{\rho q}^{(j)} = k_q \sin \alpha_j$, $k_{zq}^{(j)} = k_q \cos \alpha_j$, and $w_{jq}^{(sd)}$ and s_{jq} are the weights and locations, respectively, associated with the numerical integration rule. The index j labels the integration point.

From Eqs. (13), (16), and (18), we have

$$g_q(\mathbf{r}, \mathbf{r}') \approx \frac{i}{8\pi} \sum_{j=1}^{n_{(sd),q}} w_{jq}^{(sd)} k_{\rho q}^{(j)} H_0^{(1)}(k_{\rho q}^{(j)}|\boldsymbol{\rho} - \boldsymbol{\rho}'|) \times \exp[ik_{zq}^{(j)}(z - z')]. \quad (19)$$

The Hankel function in relation (19) can be computed efficiently for several source and observation locations through a generalization of the free-space FMM^{10,26} to an inhomogeneous plane-wave basis. The rough surface is divided into blocks lying on a plane. Sources lying in each block are represented by plane-wave expansions located at the center of each block, irrespective of the particular z location of the source. The Hankel function can then be expressed as

$$H_0^{(1)}(k_{\rho q}^{(j)}|\boldsymbol{\rho} - \boldsymbol{\rho}'|) = \frac{1}{2\pi} \int_0^{2\pi} d\phi \exp[ik_{\rho q}^{(j)}(\boldsymbol{\rho} - \boldsymbol{\rho}_b) \cdot \hat{\mathbf{s}}_q] \times \mathcal{F}(k_{\rho q}^{(j)}, \hat{\mathbf{s}}_q, \boldsymbol{\rho}_b - \boldsymbol{\rho}_a) \exp[ik_{\rho q}^{(j)}(\boldsymbol{\rho}_a - \boldsymbol{\rho}') \cdot \hat{\mathbf{s}}_q] = \frac{1}{2\pi} \sum_{j'=1}^{P_q} w_{j'q}^{(\text{fmm})} \exp\{ik_{\rho q}^{(j)}(\boldsymbol{\rho} - \boldsymbol{\rho}_b) \cdot \hat{\mathbf{s}}_{j'q}\} \times \mathcal{F}(k_{\rho q}^{(j)}, \hat{\mathbf{s}}_{j'q}, \boldsymbol{\rho}_b - \boldsymbol{\rho}_a) \exp[ik_{\rho q}^{(j)}(\boldsymbol{\rho}_a - \boldsymbol{\rho}') \cdot \hat{\mathbf{s}}_{j'q}] \quad (20a)$$

$$\mathbf{k}_q^{(j)} = k_{\rho q}^{(j)} \hat{\mathbf{s}}_{j'q} + k_{zq}^{(j)} \hat{\mathbf{z}}, \quad (20b)$$

$$\mathcal{F}(k_{\rho q}^{(j)}, \hat{\mathbf{s}}_q, \boldsymbol{\rho}_b - \boldsymbol{\rho}_a) = \sum_{p=-P_q}^{P_q} H_p^{(1)}(k_{\rho q}^{(j)}|\boldsymbol{\rho}_b - \boldsymbol{\rho}_a|) \exp\{-ip[\theta - \phi_q - \pi/2]\}, \quad (20c)$$

where P_q is the number of integration points required for the azimuthal spectral integration, $w_{j'q}^{(\text{fmm})}$ are the quadrature weights, $\boldsymbol{\rho}_a$ and $\boldsymbol{\rho}_b$ are FMM block centers, and \mathcal{F} is

the translation operator that depends on the complex wave number and spectral angles in region q and on the displacement between source and observation blocks. Also, $\hat{\mathbf{s}}_q = \hat{\mathbf{x}} \cos \phi_q + \hat{\mathbf{y}} \sin \phi_q$ and $\cos \theta = \hat{\mathbf{x}} \cdot (\boldsymbol{\rho}_b - \boldsymbol{\rho}_a) / |\boldsymbol{\rho}_b - \boldsymbol{\rho}_a|$. Finally, the MoM-matrix entries in Eq. (8) can be formally obtained in the new inhomogeneous plane-wave basis from

$$\begin{aligned} \langle \mathbf{f}_m, L_q \mathbf{j}_n \rangle &= \frac{i}{16\pi^2} \sum_{j=1}^{n_{(sd),q}} \sum_{j'=1}^{P_q} w_{jq}^{(sd)} w_{j'q}^{(fmm)} k_{\rho q}^{(j)} \\ &\times \int_S d\mathbf{r}' \mathbf{f}_m \exp[i\mathbf{k}_q^{(j)} \cdot (\mathbf{r} - \mathbf{r}_b)] \\ &\times \mathcal{F}(k_{\rho q}^{(j)}, \hat{\mathbf{s}}_{j'q}, \boldsymbol{\rho}_b - \boldsymbol{\rho}_a) \left[\bar{\mathbf{I}} - \frac{\mathbf{k}_q^{(j)} \mathbf{k}_q^{(j)}}{k_q^2} \right] \\ &\times \int_S d\mathbf{r}' \mathbf{j}_n \exp[i\mathbf{k}_q^{(j)} \cdot (\mathbf{r}_a - \mathbf{r}')] \end{aligned} \quad (21)$$

$$\begin{aligned} \langle \mathbf{f}_m, K_q \mathbf{j}_n \rangle &= -\frac{1}{16\pi^2} \sum_{j=1}^{n_{(sd),q}} \sum_{j'=1}^{P_q} w_{jq}^{(sd)} w_{j'q}^{(fmm)} k_{\rho q}^{(j)} \\ &\times \int_S d\mathbf{r} [\mathbf{f}_m \times \mathbf{k}_q^{(j)}] \exp[i\mathbf{k}_q^{(j)} \cdot (\mathbf{r} - \mathbf{r}_b)] \\ &\times \mathcal{F}(k_{\rho q}^{(j)}, \hat{\mathbf{s}}_{j'q}, \boldsymbol{\rho}_b - \boldsymbol{\rho}_a) \\ &\times \int_S d\mathbf{r}' \mathbf{j}_n \exp[i\mathbf{k}_q^{(j)} \cdot (\mathbf{r}_a - \mathbf{r}')] \end{aligned} \quad (22)$$

The above interactions are depicted schematically in Fig. 3(a). While computing a matrix-vector product, we can group source and observation terms independently (through their plane-wave spectra) rather than by individually combining the effect of single source-observer interactions. Furthermore, plane-wave spectrum information at different levels is recycled, as in standard FMMs.^{10,26} These steps result in substantial CPU time and memory savings. If exact SDP paths are used for each pair of block interactions at each level, complex interpolation operators and nondiagonal translation operators will be necessitated, thus increasing bookkeeping and memory costs. In our implementation, $\theta_c = \pi/2$ SDP's are chosen, as in our earlier work.¹⁹ However, the fact that block centers may be locally clustered around a nonzero z coordinate is utilized to factor out extraneous phase oscillations. Such a procedure potentially permits the simulation of rougher surfaces than is possible without the factorization.

In a multilevel SDFMM, the rough surface is recursively divided into blocks, through the hierarchical partitioning of a block (the parent) at a coarse level into four blocks (the children) at a finer level. As shown in Fig. 3(b) for a two-level case, plane-wave expansions are shifted to centers of parent blocks, and incoming spectra are shifted to centers of child blocks. Such an operation is termed an FMM tree traversal. Distinct translation operators and steepest-descent rules are utilized at each FMM level. For the dielectric problem, two regions with distinct material characteristics need to be considered independently, thus leading to two separate FMM trees and

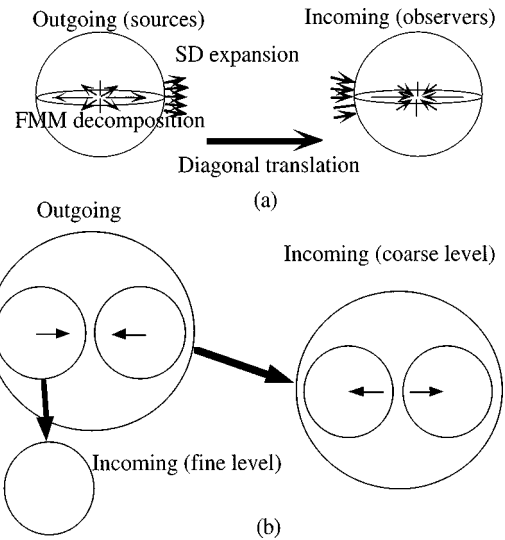


Fig. 3. Schematic description of a single-level and a two-level SDFMM: (a) SDP integration (short bold arrows), azimuthal FMM spectral integration (thinner arrows), and diagonal translation operators (long bold arrow). At an observation block, another combined SDFMM integration is used to find field values in the block. (b) In a two-level SDFMM, inhomogeneous plane-wave expansions are shifted to centers of parent blocks, and incoming plane-wave spectra are translated (thin arrows) to centers of child blocks. Two kinds of interaction are possible, one at the fine level and another at the coarser level, as shown. Distinct SDP rules, FMM integration points, and translation operators (bold arrows) are used at each level. In a multilevel SDFMM, such an approach would be continued across several levels.

tree traversals. Moreover, it can be shown that the effect of both the electric and the magnetic surface currents in a particular region can be accounted for through a single tree formation and traversal. Also, magnetic fields at the observer locations are obtained through transforming each plane-wave component of the computed electric field [see Eq. (22)].

A note is in order on the interpolation and integration methods used in the SDFMM. The SDP integration uses a simple equispaced rule to determine $w_{jq}^{(sd)}$. The number of points is determined by the required accuracy and progressively increases as the roughness of the surface increases. We derive the truncation points on the SDP by equating the integration errors for the shortest and longest distances for which the rule is used at any given level. Typically, $n_{(sd),q}$ is ~ 20 at the finest level [with blocks of area $O(4\pi^2/k_2^2)$] and diminishes at coarser levels. The truncation points progressively move inward toward the point $\alpha = \pi/2 + i0$ [see Eq. (15)] at coarser levels. Another parameter, P_q , is proportional to the minimum number of harmonics, determined by the Nyquist criterion, required for representing fields that are due to sources residing in a block of a given size.²⁷ This number is proportional to the linear dimensions of the block. To obtain P_q , a multiplicative oversampling factor is required if we are to control the error in the multipole expansion, and this oversampling rate diminishes as the block size increases. Typically, this oversampling factor is close to 3 at the finest level and steadily diminishes to

near unity after 4 levels. The integration weights $w_{j,q}^{(fmm)}$ are determined by a simple equispaced P_q point rule. Finally, the interpolation required in the multilevel SDFMM is performed independently in the SDP and FMM portions. A Lagrange interpolation is used for the SDP part, and a prolate- or Chebychev-accelerated Dirichlet interpolation is used for the FMM.²⁷

In a previous paper we rigorously showed that the computational complexity and memory requirements of the SDFMM when applied to the analysis of scattering from perfectly conducting rough surfaces are $O(N)$.¹⁹ This proof can easily be extended to the present problem involving dielectric rough surfaces. However, here we adopt a more physical approach to arrive at the same complexity measure. Consider Fig. 4, where a cross section of a two-dimensional rough surface is shown. The SDFMM blocks residing at the finest level and at a coarser level are depicted in Figs. 4(a) and 4(b), respectively. The number of inhomogeneous plane-wave components $n_{(sd),q}$ needed to perform the SDP integration at a given level is proportional to the angle that the observation region subtends at the source region; if the observation region moves closer, more points will be required in the SDP integration rule. If block sizes and minimum block separations are fixed at the finest level, then, clearly, at any coarser level, the angle subtended by an observation region is smaller than that at a finer level. In conclusion, the number of SDP integration points at any level is never larger than that at the finest level. Increasing the size of the rough surface, while keeping surface roughness and finest-level block sizes constant, will not increase the required number of SDP integration points. The cost of SDP integration per block is thus bounded, independent of the number of unknowns. In fact, the angle roughly halves each time one moves up a level; hence the number of points required for SDP integration roughly decreases initially by a factor of 2 as one moves to a coarser level, until this number saturates quickly to a small constant value.¹⁹ The remaining contribution to the computational complexity of the SDFMM arises from the multilevel two-dimensional FMM. The computational labor required per block roughly doubles as the block size doubles.^{5,7} Here block size refers to the circumference or linear dimensions of a block. The increase in computation is due to an increase in the number of sampling points ($n_{(sd),q}P_q$) required for correctly representing fields that are due to sources within a block. All four children of an SDFMM parent block are nonempty. Therefore the total computation per level diminishes by a factor of 2 at a coarser level, thus yielding an overall cost proportional to N . The use of a standard three-

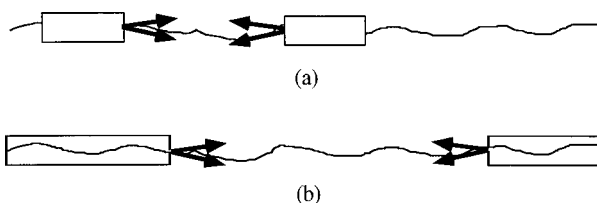


Fig. 4. SDFMM blocks at (a) the finest level (b) a coarser level. The effective angle between a source and an observation block is reduced as one goes to coarser levels.

dimensional FMM in place of the SDFMM would result in an $O(N \log N)$ complexity. This is because the total number of harmonics required increases by a factor of 4 as one goes to a coarser level (proportional to the surface area of the block). Thus the computation per level remains constant and proportional to N , thus making the overall cost over $\log N$ levels scale as $O(N \log N)$. Physically, the extra $\log N$ term appears because a standard FMM does not exploit the angle reduction discussed above and illustrated in Fig. 4.

4. SIMULATION RESULTS

In this section several numerical results are presented that demonstrate the efficacy of the SDFMM in analyzing scattering from dielectric rough surfaces. The computing platform used is a single R8000 processor on an SGI Power Challenge, with 2 Gbytes of RAM and an average throughput of 60 MFlops.

To validate the SDFMM, it is applied to the problem of scattering from a relatively small rough surface, and the RCS obtained is compared with that from a standard MoM. The surface dimensions are $5.5\lambda^2$, with $\sigma = 0.4\lambda$ and $l_c = 1.0\lambda$, where λ is the free-space wavelength. The dielectric constant of region 2 is $\epsilon_2 = 3 + 0.1i$, thus making the surface dimensions equal to $16.4\lambda^2$ in the dielectric. In this and all other numerical examples shown in this section, finest-level blocks of size $0.15\lambda \times 0.15\lambda$ are used in the SDFMM, unless otherwise stated. Also, we assume throughout this section that $\epsilon_1 = 1$, i.e., that the incident wave impinges on the interface from a free-space region. The small rough-surface problem involves 4,485 unknowns. A normally incident Gaussian beam ($\theta = 0$) is used as the excitation. For this and the other numerical examples, the electric-field vectors of the components of the Gaussian beam are polarized in the x - z plane. The angle θ specifies the angle between the beam and the z axis, with negative values indicating an incident beam with a positive x component. A transpose-free quasi-minimal residual iterative solver²⁸ is used with both the SDFMM and the MoM. As can be seen from Fig. 5, the RCS results are in very good agreement.

We examine the CPU time and memory requirements of the SDFMM by applying it to progressively larger problems. The rough surfaces used for this purpose are characterized by $\sigma = 0.4\lambda$ and $l_c = 1.5\lambda$ and form the interface between half-spaces composed of free space and a dielectric with $\epsilon_2 = 2$. The SDP integration rules used in this case are designed for surfaces that have a maximum roughness of $\sigma = 1.0\lambda$, and therefore the results for memory and time usage are representative for all surfaces that have any smaller roughness. Figure 6 depicts the CPU time required for a matrix-vector product. The CPU time required for direct matrix-vector multiplication, in a standard iterative solution of an MoM system of equations, scales as $O(N^2)$. The SDFMM, on the other hand, requires CPU time proportional only to $O(N)$, as suggested in the previous section. The break-even point is near 33,000 unknowns. Nevertheless, it is still advantageous to employ the SDFMM for much smaller problems, as will be explained later in this section.

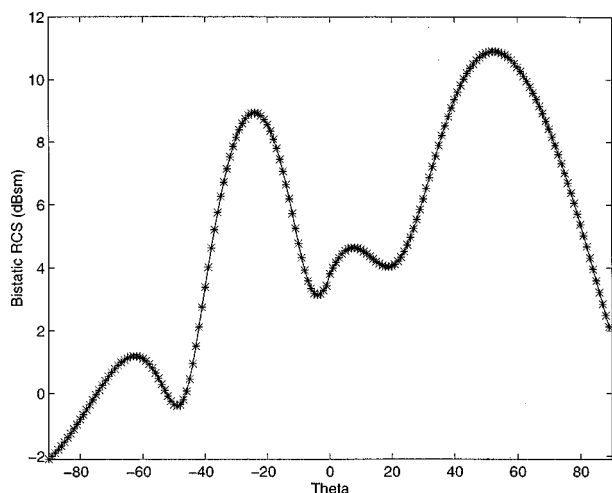


Fig. 5. Comparison of RCS results obtained by MoM (solid curve) and SDFMM (*). The dielectric rough surface is of dimensions $5.5\lambda^2$, with $\sigma = 0.4\lambda$ and $l_c = 1.0\lambda$, where λ is the free-space wavelength. The dielectric constant is $\epsilon_2 = 3 + 0.1i$, thus making the surface dimensions equal to $16.4\lambda^2$ in the dielectric. A finest-level box size of $0.15\lambda \times 0.15\lambda$ is used in the SDFMM.

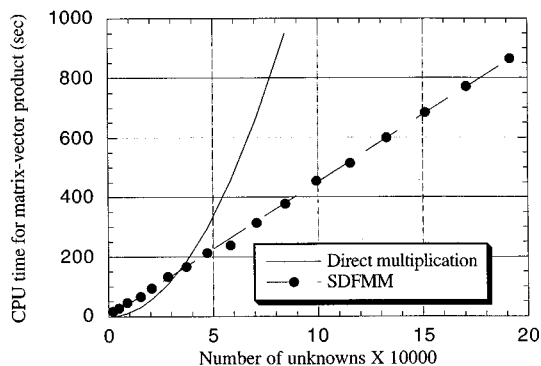


Fig. 6. Matrix-vector product times for direct multiplication and the SDFMM, as a function of problem size.

A standard iterative MoM solution entails storage of the entire MoM matrix. This leads to prohibitively large $O(N^2)$ memory requirements, as can be seen from Fig. 7. If we use a computer with 2 Gbytes of memory, the largest solvable problem would have approximately $N = 16,000$ unknowns. The SDFMM has far more economical memory requirements, scaling as $O(N)$. A problem involving $N = 191,000$ unknowns can be accommodated in 1.8 Gbytes of memory, as is clear from Fig. 7.

The overall CPU time required for solving the integral equation consists of two dominant portions. One is proportional to the product of the cost of a matrix-vector and the number of iterative steps required. The second is the initial setup time, which in the case of a standard MoM is the matrix-fill time, while for the SDFMM, it is the matrix-fill time for the near-field part \bar{Z} and the inhomogeneous plane-wave projection generation time for the far-field portion. As shown in Fig. 8, the setup time rises extremely steeply, with an $O(N^2)$ growth for the standard MoM, and is as high as 200 min for a moderately sized 10,000 unknown problem. The SDFMM has a far more gradual $O(N)$ growth. For small rough-surface prob-

lems, the setup time for the standard MoM can far exceed the iterative solution time. Therefore, even for small problems, the overall solution time can be much larger for the MoM than for the SDFMM. Thus it is advantageous to use the SDFMM even below the break-even point. In practice the SDFMM works faster than the MoM for surfaces requiring $\sim N = 5,000$ or more unknowns. The speedup and memory savings become dramatic as the problem size increases; for an $N = 191,530$ unknown case, a standard iterative MoM solution would entail practically impossible CPU time requirements of 80 min per matrix-vector product and 1,200 h for matrix fill and would require 325 Gbytes of memory. The SDFMM correspondingly needs only ~ 14 min for a matrix-vector product, 3 h for setup, and 2 Gbytes of memory.

We have observed that using finest-level blocks of size $0.3\lambda \times 0.3\lambda$ leads to matrix-vector products that are nearly twice as fast as those with finest-level blocks half this size. However, this advantage is offset by both memory requirements and setup times growing by a factor of 3 or more.

The SDFMM has been applied to analyze scattering from large dielectric rough surfaces, and three results are depicted in Figs. 9, 10, and 11 for single surface realizations. The first surface has an area of $162\lambda^2$, with $\sigma = 0.2\lambda$ and $l_c = 1.5\lambda$.

A Gaussian beam is incident at $\theta = -15^\circ$, and the dielectric constant of the surface is $\epsilon_2 = 2$, thus making the surface dimensions equal to $324\lambda^2$ in the dielectric. The surface is modeled with 151,046 unknowns. The copolarized bistatic RCS in the $x-z$ plane is shown in Fig. 9.

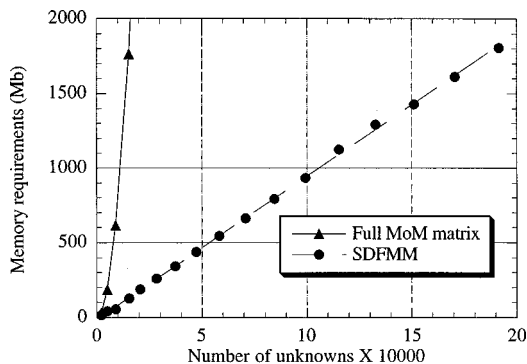


Fig. 7. Memory requirements for the standard MoM and the SDFMM, as a function of problem size.

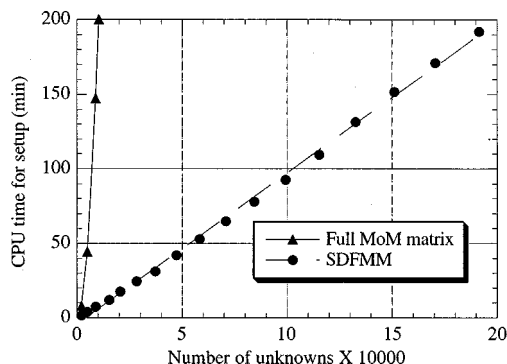


Fig. 8. Comparison of matrix-fill time for the standard MoM and setup time for the SDFMM, as a function of problem size.

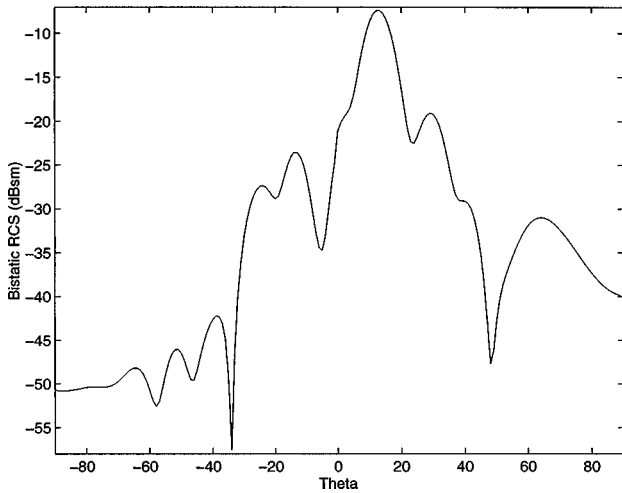


Fig. 9. Copolarized bistatic RCS for a dielectric rough surface of area $162\lambda^2$, with $\sigma = 0.2\lambda$ and $l_c = 1.5\lambda$, where λ is the free-space wavelength.

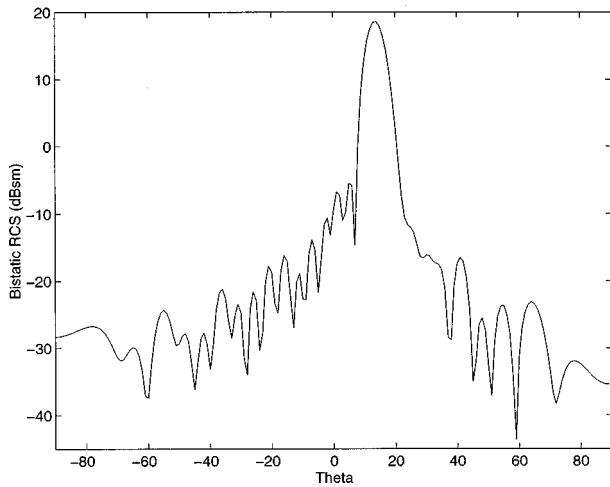


Fig. 10. Copolarized bistatic RCS for a dielectric rough surface of area $205\lambda^2$, with $\sigma = 0.05\lambda$ and $l_c = 1.0\lambda$, where λ is the free-space wavelength.

The specular peak is visible alongside other smaller ones produced as a result of noncoherent scattering from the rough surface. A larger surface is modeled to obtain the RCS depicted in Fig. 10. In this case the area is $205\lambda^2$. The surface is only mildly rough with $\sigma = 0.05\lambda$ and $l_c = 1.0\lambda$. A Gaussian beam is again incident at $\theta = -15^\circ$, and $\epsilon_2 = 2$, thus making the surface dimensions equal to $410\lambda^2$ in the dielectric. This problem requires 191,530 unknowns. The specular peak is relatively much stronger than in Fig. 9, which is expected, since the surface has a relatively smooth nature. Another surface of the same area, but with $\sigma = 0.4\lambda$ and $l_c = 1.5\lambda$, is modeled, and the RCS is shown in Fig. 11. A Gaussian beam is incident at $\theta = -45^\circ$. Here, owing to the moderately large roughness, there are several scattering peaks that are strong, including the specular one. The added roughness of this surface manifests itself in the number of iterations required for the TFQMR iterative solver to converge; 142 iterations are required as compared with 103 for the previous example.

To demonstrate the suitability of the SDFMM for carrying out Monte Carlo simulations, 50 moderately large rough surfaces (each modeled with 20,650 unknowns) are analyzed, and the variance of the scattered field is used to predict the bistatic scattering coefficient. It should be noted that for a truly useful Monte Carlo simulation, one should use a larger number of realizations as well as larger surfaces. However, this example serves to demonstrate the capability of the SDFMM on our laboratory computational platform, which does not permit the solution of multiple large problems in reasonable times. The example considered here uses surfaces of area $22.3\lambda^2$, with $\sigma = 0.4\lambda$ and $l_c = 1.5\lambda$, where λ is the free-space wavelength as before. The dielectric constant $\epsilon_2 = 2$, thus making the surface area $44.6\lambda^2$ in the dielectric. A Gaussian beam is incident at $\theta = -45^\circ$. Even with this small number of samples and small surface size, back-scattering enhancement is visible in the copolarized scattering coefficient as depicted in Fig. 12. Finest-level boxes of size $0.3\lambda \times 0.3\lambda$ were used to accelerate the

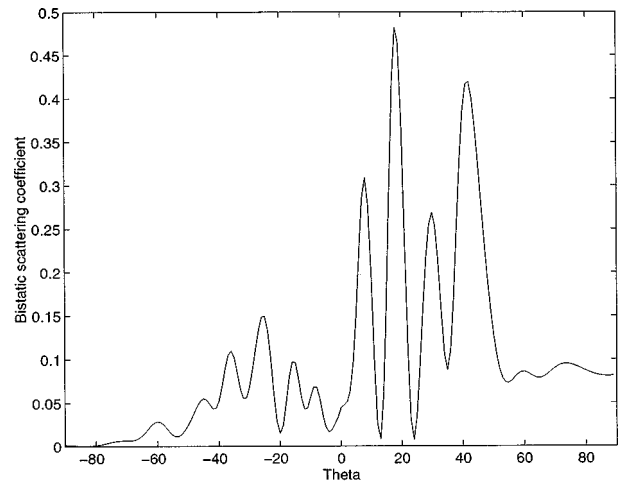


Fig. 11. Copolarized bistatic RCS for a dielectric rough surface of area $205\lambda^2$, with $\sigma = 0.4\lambda$ and $l_c = 1.5\lambda$, where λ is the free-space wavelength.

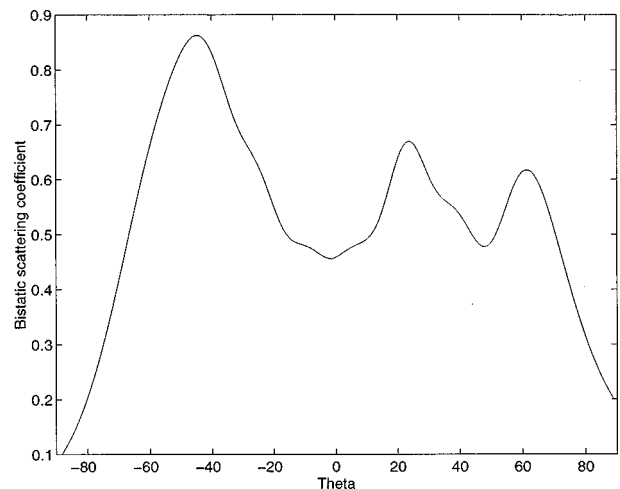


Fig. 12. Copolarized bistatic scattering coefficient obtained through a Monte Carlo simulation involving 50 realizations of rough surfaces of size $22.28\lambda^2$, with $\sigma = 0.4\lambda$ and $l_c = 1.5\lambda$, where λ is the free-space wavelength.

matrix-vector product computation. Each matrix-vector product required 46 sec, and an average of 96 TFQMR iterations were needed per surface.

5. CONCLUSIONS

A new multilevel algorithm, the SDFMM, has been shown to permit the rapid analysis of scattering from dielectric rough surfaces. This method has $O(N)$ CPU time and memory requirements and is sufficiently fast to permit large-scale rough-surface simulations within reasonable times. The technique is rigorous and permits a tradeoff between accuracy and efficiency. The application of the SDFMM to a variety of dielectric rough-surface problems is being studied; these include the analysis of rough absorbers for infrared detectors and optical devices and the study of solar panels. Further generalizations to microwave circuits with finite dielectric substrates and ground planes are currently under development. Advanced preconditioning techniques for reducing the number of iterations required for convergence are also being examined.

ACKNOWLEDGMENT

The work presented in this paper was supported in part by a grant from the U.S. Air Force Office of Scientific Research through the Multi University Research Initiative Program under contract F49620-96-1-0025.

*Present address, Ansoft Corporation, Four Station Square, Suite 660, Pittsburgh, Pa. 15219; phone, 412-261-3200, ext. 144; fax, 412-471-9427; e-mail, vikram@ansoft.com.

[†]E. Michielssen's e-mail address is michiels@decwa.ece.uiuc.edu.

REFERENCES

1. See *Proceedings of the Workshop on Rough Surface Scattering and Related Phenomena* (Napa Valley Lodge, Yountville, Calif., 1996).
2. A. Ishimaru, *Wave Propagation and Scattering in Random Media* (Academic, New York, 1978).
3. V. Rokhlin, "Rapid solution of integral equations of scattering theory in two dimensions," *J. Comput. Phys.* **36**, 414–439 (1990).
4. N. Engheta, W. D. Murphy, V. Rokhlin, and M. S. Vassiliou, "The fast multipole method (FMM) for electromagnetic scattering problems," *IEEE Trans. Antennas Propag.* **40**, 634–641 (1992).
5. R. Coifman, V. Rokhlin, and S. Wandzura, "The fast multipole method for the wave equation: a pedestrian description," *IEEE Antennas Propag. Mag.* **35**, 7–12 (1993).
6. C. C. Lu and W. C. Chew, "A multilevel algorithm for solving a boundary integral equation of wave scattering," *Microwave Opt. Technol. Lett.* **7**, 466–470 (1994).
7. J. M. Song and W. C. Chew, "Multilevel fast-multipole algorithm for solving combined field integral equations of electromagnetic scattering," *Microwave Opt. Technol. Lett.* **10**, 14–19 (1995).
8. R. L. Wagner and W. C. Chew, "A ray-propagation fast multipole algorithm," *Microwave Opt. Technol. Lett.* **7**, 435–438 (1994).
9. M. A. Epton and B. Dembart, "Multipole translation theory for the three-dimensional Laplace and Helmholtz equations," *SIAM J. Sci. Comput.* **16**, 865–897 (1995).
10. C. C. Lu and W. C. Chew, "Fast algorithm for solving hybrid integral equations," *IEE Proc. H* **140**, 455–460 (1993).
11. E. Michielssen and A. Boag, "A multilevel matrix decomposition algorithm for analyzing scattering from large structures," *IEEE Trans. Antennas Propag.* **44**, 1086–1093 (1996).
12. C. H. Chan and L. S. Tsang, "A sparse-matrix canonical-grid method for scattering by many scatterers," *Microwave Opt. Technol. Lett.* **8**, 114–118 (1995).
13. E. Bleszynski, M. Bleszynski, and T. Jaroszewicz, "A fast integral-equation solver for electromagnetic scattering problems," in *Proceedings of the IEEE/APS International Symposium, Seattle, Washington* (Institute of Electrical and Electronics Engineers, Piscataway, N. J., 1994), pp. 416–419.
14. J. T. Johnson, L. Tsang, R. T. Shin, K. Pak, C. H. Chan, A. Ishimaru, and Y. Kuga, "Backscattering enhancement of electromagnetic waves from two-dimensional perfectly conducting random rough surfaces—a comparison of Monte Carlo simulations with experimental data," *IEEE Trans. Antennas Propag.* **44**, 748–756 (1996).
15. K. Pak, L. Tsang, C. Chan, J. Johnson, and Q. Li, "Scattering of electromagnetic waves in large-scale rough surface problems based on the sparse-matrix canonical-grid method," in *Proceedings of the 13th Annual Review of Progress in Applied Computational Electromagnetics* (Applied Computational Electromagnetics Society, Monterey, Calif., 1997).
16. R. L. Wagner, J. Song, and W. Chew, "Monte Carlo simulation of electromagnetic scattering from two-dimensional random rough surfaces," *IEEE Trans. Antennas Propag.* **45**, 235–245 (1997).
17. D. A. Kapp and G. Brown, "A new numerical method for rough-surface scattering calculations," *IEEE Trans. Antennas Propag.* **44**, 711–721 (1996).
18. E. Michielssen, A. Boag, and W. C. Chew, "Scattering from elongated objects: direct solution in $O(N \log^2 N)$ operations," *IEE Proc. Microwaves Antennas Propag.* **143**, 277–283 (1996).
19. V. Jandhyala, E. Michielssen, B. Shanker, and W. Chew, "A combined steepest descent-fast multipole algorithm for the fast analysis of three-dimensional scattering by rough surfaces," *Tech. Rep. CCEM-3-97* (Center for Computational Electromagnetics, University of Illinois, Urbana, 1997).
20. L. Medgyesi-Mitschang, J. Putnam, and M. Gedera, "Generalized method of moments for three-dimensional penetrable scatterers," *J. Opt. Soc. Am. A* **12**, 1383–1398 (1994).
21. P. Tran and A. A. Maradudin, "The scattering of electromagnetic waves from a randomly rough 2-D metallic surface," *Opt. Commun.* **110**, 269–273 (1994).
22. K. Umashankar, A. Taflove, and S. Rao, "Electromagnetic scattering by arbitrary shaped three-dimensional homogeneous lossy dielectric object," *IEEE Trans. Antennas Propag.* **34**, 758–765 (1986).
23. P. Tran, V. Celli, and A. A. Maradudin, "Electromagnetic scattering from a two-dimensional, randomly rough, perfectly conducting surface: iterative methods," *J. Opt. Soc. Am. A* **11**, 1686–1689 (1994).
24. S. M. Rao, D. R. Wilton, and A. Glisson, "Electromagnetic scattering by surfaces of arbitrary shape," *IEEE Trans. Antennas Propag.* **30**, 409–418 (1982).
25. W. C. Chew, *Waves and Fields in Inhomogeneous Media* (Institute of Electrical and Electronics Engineers, Piscataway, N. J., 1995).
26. J. Rahola, "Efficient solution of linear equations in electromagnetic scattering calculations," *Tech. Rep. CSC Research Reports R06/96* (Center for Scientific Computing, Espoo, Finland, 1996).
27. O. Bucci, C. Gennarelli, and C. Savarese, "Optimal interpolation of radiated fields over a sphere," *IEEE Trans. Antennas Propag.* **39**, 1633–1643 (1991).
28. J. Volakis, "EM programmer's notebook," *IEEE Antennas Propag. Mag.* **37**, 94–100 (1995).